WISHE-Moisture Mode in an Aquaplanet Simulation

Xiaoming Shi[1,2] [ID]**, Daehyun Kim[3]** [ID]**, Ángel F. Adames[4]** [ID]**, and Jai Sukhatme[5]**

[1]Civil and Environmental Engineering, University of California, Berkeley, CA, USA, [2]Now at Division of Environment and Sustainability, Department of Civil and Environmental Engineering, Hong University of Science and Technology, Hong Kong, [3]Department of Atmospheric Sciences, University of Washington, Seattle, WA, USA, [4]Department of Climate and Space Science and Engineering, University of Michigan, Ann Arbor, MI, USA, [5]Centre for Atmospheric and Oceanic Sciences, Indian Institute of Science, Bangalore, India

Abstract This study aims to understand the nature of the tropical intraseasonal oscillations (ISOs) in an aquaplanet simulation performed using Geophysical Fluid Dynamics Laboratory's AM2.1 with a uniform sea surface temperature within the deep tropics. The simulated ISO resembles the observed Madden-Julian Oscillation in that the spectral peak in precipitation appears at zonal wave number 1 and a period of ~60 days. Vertically integrated moist static energy budget of the simulated ISO shows that enhanced latent heat flux to the east of anomalously active convection causes eastward propagation of the ISO mode, which is weakly opposed by horizontal moisture advection. A series of mechanism denial experiments are conducted either by homogenizing select variables—surface wind stress, longwave radiative heating, and surface evaporation—with their zonal means from the control simulation or by suppressing free-tropospheric moisture variation. Results of the mechanism denial experiments show that the simulated ISO disappears when the interactive surface evaporation is disabled, suggesting that the wind-induced surface heat exchange (WISHE) mechanism is essential to the simulated ISO. Longwave cloud-radiation feedbacks and moisture-convection feedbacks affect horizontal scale and phase speed of the simulated ISO, respectively. Our results strongly suggest that the simulated ISO is the linear WISHE-moisture mode of Fuchs and Raymond under horizontally uniform boundary conditions.

1. Introduction

Aquaplanet simulations—running numerical models of the atmosphere on a water-covered Earth—are in a unique position in the hierarchy of atmospheric modeling systems and have served an important role in understanding the dynamics of various atmospheric phenomena (Blackburn & Hoskins, 2013). The tropical intraseasonal oscillation (ISO) is no exception in this regard. The first aquaplanet simulation using an atmospheric general circulation model was performed by Hayashi and Sumi (1986), who observed a 30- to 40-day tropical ISO in their simulation. Their results demonstrated that aquaplanet simulations are a useful method to study the tropical ISO. Since then, many modeling studies of the tropical ISO have employed the aquaplanet configuration (e.g., Andersen & Kuang, 2012; Arnold et al., 2013; Das et al., 2016; Grabowski, 2003; Hsu et al., 2014; Kang et al., 2013; Y.-J. Kim et al., 2008; Lee et al., 2001; Leroux et al., 2016; Swinbank et al., 1988). Readers are referred to Leroux et al. (2016) for a brief review of previous aquaplanet modeling studies on the tropical intraseasonal variability.

The Madden-Julian oscillation (MJO, Madden & Julian, 1971, 1972) is the dominant mode of tropical intraseasonal variability whose influence on the global weather-climate system is well documented (Zhang, 2013). While the salient features of the MJO—planetary zonal scale, 30- to 60-day period, and eastward propagation at ~5 m/s over the Indo-Pacific warm pool—have been well known for many decades, our understanding of the MJO is still unsatisfactory.

One of the distinguishing features of the MJO is the strong spatial and temporal coupling between tropospheric water vapor and latent heat release (Myers & Waliser, 2003; Yasunaga & Mapes, 2012), which is central to multiple recent theories for the MJO (Adames & Kim, 2016; Fuchs & Raymond, 2017, FR17 hereafter; Majda & Stechmann, 2009; Sobel & Maloney, 2012, 2013; Wang & Chen, 2017). In the so-called "moisture mode theories", the processes that determine the growth and propagation of the large-scale moisture envelope also explain those of the MJO. With the common core concept, the different linear theories of the moisture mode emphasize different processes for MJO propagation, maintenance, and scale selection. The processes that are suggested as key destabilization and planetary-scale selection mechanism of the MJO include a negative

gross moist stability (GMS) or the moisture mode instability (Raymond & Fuchs, 2009), the cloud-radiative feedbacks (Adames & Kim, 2016), and wind-induced surface heat exchange (WISHE; Emanuel, 1987; Fuchs & Raymond, 2017; Neelin et al., 1987). Similarly, for the processes that drive the propagation of the MJO, horizontal moisture advection (Adames & Kim, 2016), frictional moisture convergence (Wang & Chen, 2017), and WISHE (Fuchs & Raymond, 2017) have been emphasized.

All these theories share the common feature that they are based on zonally symmetric mean states. Horizontally, homogenous mean states without zonal or meridional SST gradients are sometimes used (Fuchs & Raymond, 2017). Simulations on a zonally symmetric aquaplanet could provide a useful framework to test the importance of the key mechanisms suggested by different theories to simulated intraseasonal variability since the modeled mean state resembles those assumed by linear theory.

Many previous aquaplanet modeling studies have aimed at providing useful insights into the dynamics of the MJO. Inspired by the moisture mode theory, moist static energy (MSE) budget of ISOs simulated in aquaplanet simulations are analyzed. Maloney et al. (2010) showed based on the MSE budget that WISHE and horizontal moisture advection were key to the destabilization and eastward propagation of an MJO-like mode in their simulation. Andersen and Kuang (2012) performed aquaplanet simulation with the Superparameterized Community Atmospheric Model (SPCAM) and suggested that the longwave cloud-radiation feedbacks, which were the main source of MSE, played a key role in the growth of the MJO-like disturbance in their simulations. Simulations of a rotating radiative-convective equilibrium simulation by Arnold and Randall (2015) further supported the role of longwave radiative heating in the maintenance of the MJO. The aquaplanet modeling studies have often been accompanied by mechanism denial experiments (Chao & Chen, 2001; Grabowski, 2003; D. Kim et al., 2011; Lee et al., 2001; Maloney & Sobel, 2004; Sobel et al., 2010). For example, Lee et al. (2001) specified the zonal mean net radiative heating rate and found that cloud-radiation interaction had negative effects on the tropical intraseasonal variability by effectively exciting small-scale disturbances. Grabowski (2003) tested the role of WISHE and cloud-radiation interaction in the maintenance of an MJO-like disturbance and found that WISHE had a moderate importance in the development of the disturbance, while cloud-radiation interaction played a minor role.

The current study is motivated by the results of a global rotating radiative-convective equilibrium simulation performed by Shi and Bretherton (2014) using the Geophysical Fluid Dynamics Laboratory (GFDL)'s AM2.1 (Anderson et al., 2004). In their simulation, AM2.1 was driven by globally uniform sea surface temperature (SST) on an aquaplanet. Shi and Bretherton (2014) unexpectedly found an MJO-like intraseasonal variability in their simulation. It was unexpected because it has been documented that AM2.1 cannot realistically simulate the MJO with the observed SST and the full geography (D. Kim et al., 2011). The goal of the current work is to illuminate the dynamics of the simulated ISO mode by analyzing the moist static energy budget of the mode and also by performing a series of mechanism denial simulations.

The structure of the current document is as follows. Section 3 describes the simulations performed, including the mechanism denial experiments. In section 4, we examine vertically resolved moisture budget of the simulated ISO mode. Section 5 presents the results of the mechanism denial simulations. A summary and discussions on the nature of the simulated ISO mode are given in section 6.

2. Model and Simulation Design

2.1. Numerical Model

The atmospheric general circulation model used in this study is the GFDL's AM2.1 (Anderson et al., 2004). Standard physics schemes and parameters of AM2.1 are adopted in our simulations. AM2.1 has a finite-volume dynamical core on a latitude-longitude grid (Lin, 2004), which in our simulations has a resolution of 1 latitude by 1.25 longitude, with 24 vertical levels. As detailed in Anderson et al. (2004), clouds and precipitation in AM2.1 are parameterized with the aid of prognostic variables for the cloud fraction and the specific humidities of cloud liquid water and cloud ice, and grid-scale fluxes of rain and snow are computed diagnostically from these prognostic fields (Rotstayn, 1997; Rotstayn et al., 2000; Tiedtke, 1993). Cumulus convection is represented by the Relaxed Arakawa-Schubert formulation of Moorthi and Suarez (1992). Readers interested in details of AM2.1 physics schemes or dynamics are referred to Anderson et al. (2004), and references therein.
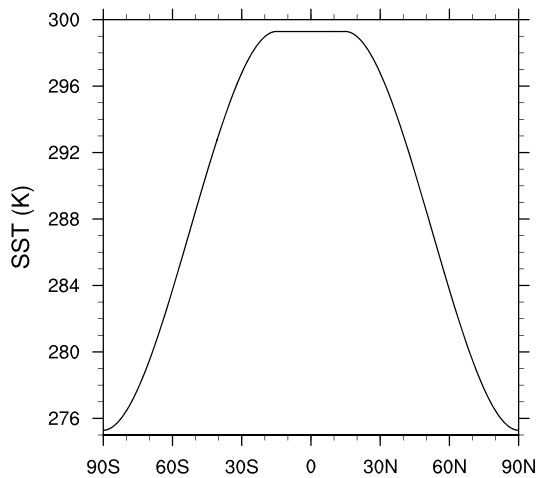
Figure 1. Prescribed sea surface temperature (SST) in the simulations.

2.2. Control Simulation

The SST for our control aquaplanet simulation is uniform in the deep tropics between 15°S and 15°N and shows a gradual transition to 2°C between 15°S/N to the South/North Poles (Figure 1). This prescribed SST is zonally invariant. Note that by using this SST distribution, we attempt to reproduce the simulation analyzed by Shi and Bretherton (2014), except that we impose a meridional SST gradient poleward of 15°S/N in order to make the simulation more relevant to the Earth's climate.

2.3. Mechanism Denial Experiments

Based on the control simulation, we performed a series of mechanism denial experiments, in which certain feedback processes are disabled by muting the variability of key variables. Here in each experiment, the variability of a select field is eliminated or suppressed in the deep tropics between 15°S and 15°N. The target feedback process and experimental design of the mechanism denial experiments are described below.

(a) Nudge_q, Fixed_q

In the Nudge_q and Fixed_q simulations, perturbations in specific humidity q in the deep tropics above 850 hPa is *nudged* toward and *fixed* to the desired vertical profile, respectively. The reference profile is obtained from the control run. The Nudge_q experiment uses a 60-hr nudging time scale. By artificially suppressing and inhibiting free-tropospheric moisture variability, the Nudge_q and Fixed_q experiments test the role of moisture-wave coupling in the simulated ISO mode.

(b) Fixed_tau

In the Fixed_tau experiment, the zonal mean surface wind stress from the control simulation is prescribed in the deep tropics. This disables the interaction of large-scale circulation with the friction-induced boundary layer convergence, which has been proposed a key process to MJO's eastward propagation (Hsu & Li, 2012; Wang, 1988; Wang & Li, 1994; Wang & Rui, 1990).

(c) Fixed_Q_{LW}

As in the Fixed_tau experiment, the zonal mean longwave radiative heating rate is obtained from the control simulation and prescribed in the Fixed_Q_{LW} experiment. Therefore, the longwave cloud-radiation feedbacks are turned off in this simulation. The interaction of longwave cooling with MJO-induced moisture and cloud anomalies have been suggested as the dominant maintenance mechanism of the MJO (Adames & Kim, 2016; Andersen & Kuang, 2012; Arnold & Randall, 2015; Bony & Emanuel, 2005; Crueger & Stevens, 2015).

(d) Fixed_LH

In the Fixed_LH experiment, the interaction between large-scale circulation and surface latent heat flux is disabled by prescribing surface latent heat flux, which is obtained from the control simulation as the zonal mean value. This experiment tests the influence of wind-evaporation feedback or WISHE mechanism (Emanuel, 1987, 1993; Fuchs & Raymond, 2017; Neelin et al., 1987; Yano & Emanuel, 1991) on the MJO-like ISO mode.

Each experiment is run for 12 years. The first 2-year data are discarded as spin-up, and the last 10-year data are retained for analysis. Model data are archived with daily intervals for the analysis.

2.4. Regression Maps

In each simulation, we define intraseasonal variability (ISV) index as the 20- to 100-day band-pass filtered precipitation in a $10° \times 10°$ square region centered at the equator. The time series of ISV index is used to produce regression maps of other variables. We did not choose time/wave number-filtered anomalies to create the ISV index because the wave number, frequency, and propagation direction of the dominant mode change significantly from one experiment to another.

Following Adames and Wallace (2014), the regression map for each variable is obtained through the equation.
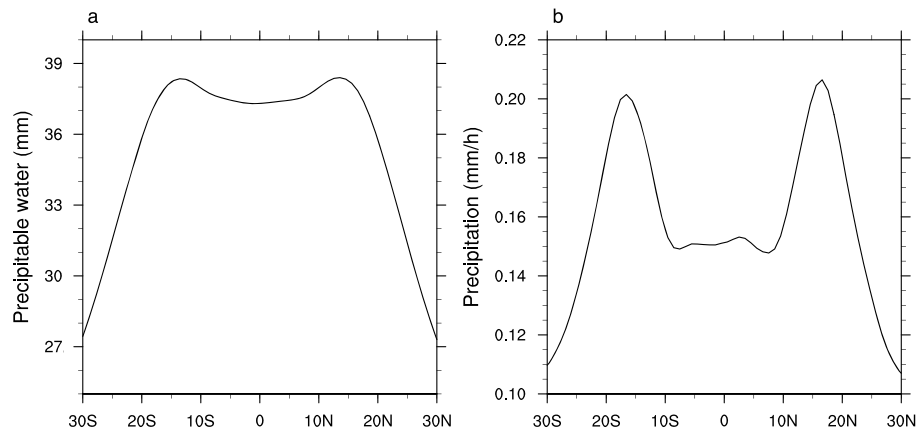
Figure 2. Time mean, zonal mean distribution of (a) precipitable water (PW, mm) and (b) precipitation rate (mm/hr) in the control simulation.

$$\mathbf{D} = \mathbf{S}\,\mathbf{P}^{T}/N \tag{1}$$

where $\mathbf{D}$ is the regression pattern, in dimensional units, for a two-dimensional matrix $\mathbf{S}$ that represents a variable field S, $\mathbf{P}$ is a standardized time series of the ISV index, and N is the sample size in days. The regression maps correspond to 1-standard-deviation anomalies.

3. MJO-Like ISO Mode in the Control Simulation

In this section, we examine the mean state and the intraseasonal variability in the control simulation. Figure 2 shows the distribution of mean precipitation and precipitable water in the control simulation. The mean precipitation exhibits two Inter Tropical Convergence Zones (ITCZs) at around 15°N/S, respectively. Except near the latitude of the ITCZs, mean moisture in the deep tropics exhibits very weak gradient in the meridional direction. The very weak horizontal moisture gradient suggests that the advection of mean moisture by perturbation winds would be small.

Figure 3 shows the space-time spectrum of equatorial precipitation in the control simulation. Only the spectrum of the symmetric component is shown as it dominates the antisymmetric component. Tropical variability in the control run is dominated by a wave number-1 mode that propagates eastward and has a period of about 60 days, resembling that of the observed MJO. Hereafter, we will call this MJO-like mode the aquaplanet ISO mode, or simply the ISO mode. It is also worthwhile to mention that due to strong surface easterlies (not shown), the power spectrum features a pronounced westward propagating signal.

The horizontal structure of the ISO mode in the control simulation is presented in Figure 4, which shows regression maps of precipitation, 850-hPa wind, 850-hPa streamfunction, and evaporation. All fields are dominated by wave number-1 structures. Near the equator, the low tropospheric wind anomalies exhibit strong convergence at the l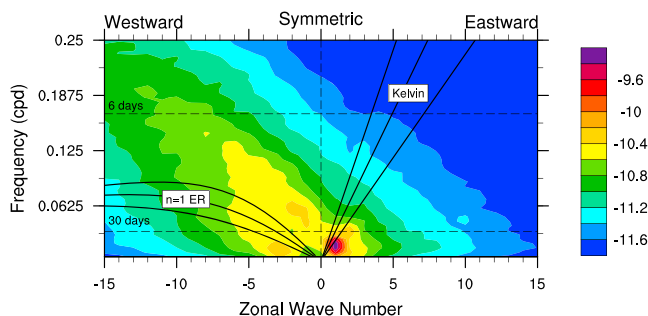ocation of maximum precipitation anomaly. This low-level convergence is much stronger in the zonal direction than in the meridional direction. The meridional wind anomalies are overall much weaker than the zonal wind anomalies. Away from the equator, streamfunction anomalies indicate a poleward flow at the longitude of and to the west of enhanced convection. This differs from the structure of the MJO in the reanalysis products, which has a poleward anomalous flow to the east of enhanced convection (e.g., Adames & Wallace, 2015; D. Kim et al., 2014). Figure 4b shows evaporation anomalies in contours, and the closed contour at 90°W and on the equator indicates the maximum. It shows that surface evaporation anomalies lead precipitation anomalies by about 90° in longitude, suggesting that enhanced surface latent heat flux to the east of enhanced convection may be responsible
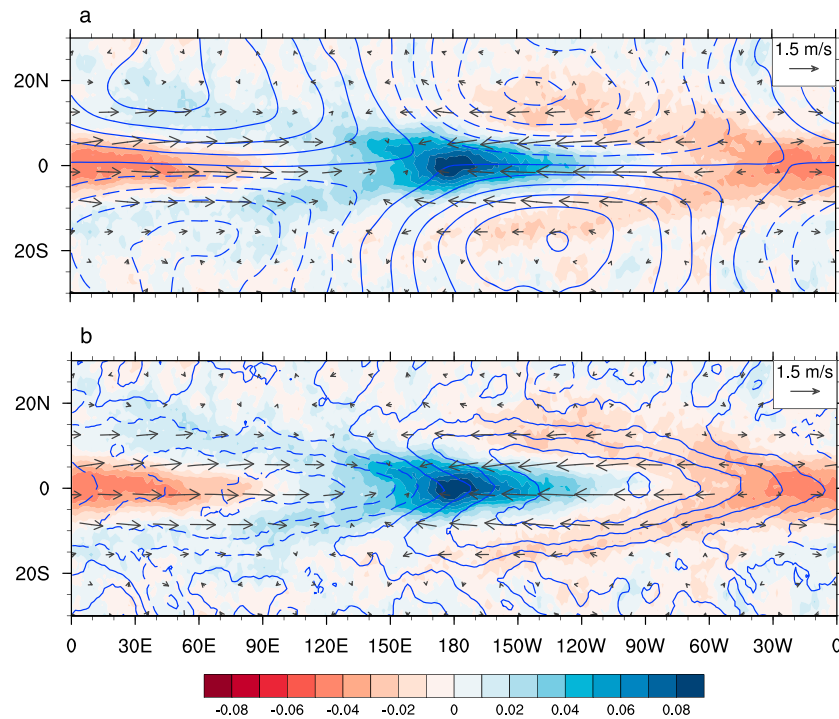

Figure 3. Space-time spectrum of the symmetric component of precipitation within between 15°S and 15°N in the control simulation.

Figure 4. The regression map of precipitation (color), 850-hPa wind (vectors), 850-hPa streamfunction (contours in a) and surface evaporation (contours in b) onto the intraseasonal variability index time series in the control simulations. Dashed contours indicate negative values. Units for precipitation is mm/hr. Contour interval for evaporation is 0.004 mm/hr.

for the eastward propagation of the ISO mode. This phase relationship between precipitation and surface evaporation in the aquaplanet-simulated ISO mode contrasts with that of the observed MJO, in which evaporation is enhanced to the west of convection, not to the east (Shinoda et al., 1998). Interestingly, both precipitation and surface evaporation show *swallowtails* to the west of maximum anomalies.

Figure 5 shows the vertical structure of the aquaplanet ISO mode. The maximum positive moisture anomalies appear at the location of the maximum precipitation anomalies, suggesting a strong moisture-convection coupling in the ISO mode. Moisture anomalies tilt slightly westward with height. Due to the rearward tilting, moisture anomalies in the upper troposphere slightly lag precipitation anomalies. The mass flux anomalies show a strong low-level convergence and strong upper-level divergence slightly to the west of enhanced
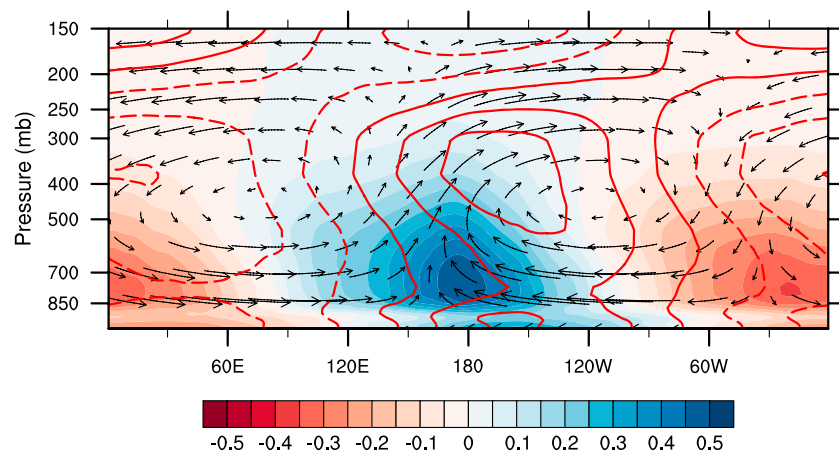

Figure 5. Regression map of mass flux (ρu and ρw), specific humidity (q; color shading) and temperature (T; contours) within 5°S and 5°N onto the time series of ISV index in the control simulation. The unit of q is g/kg. Contour interval for T is 0.1 K. ρw is multiplied by a factor of 250 for better visualization.

convection. Positive temperature anomalies are located to the east of positive moisture anomalies and tilt westward with height, showing that temperature anomalies are partly in phase with convection. This partly in-phase relation between temperature field and convection (diabatic heating) has been suggested as the destabilization mechanism of the WISHE-driven mode (Emanuel et al., 1994).

In order to understand the time evolution of the moisture anomalies, which are tightly coupled to convection, the column-integrated MSE budget of the ISO mode is examined. The tendency of anomalous MSE is determined as follows:

$$\frac{\partial h'}{\partial t} = -\langle V \cdot \nabla h \rangle' - \left\langle \omega \frac{\partial h}{\partial p} \right\rangle' + LH' + SH' + LW' + SW',$$

(2)

where h is MSE, LH and SH represent surface latent and sensible heat flux, respectively, and LW and SW represent column-integrated longwave and shortwave radiative heating, respectively. The primes in equation (2) correspond to 20- to 100-day filtered fields and the angled brackets represent column integration. The tendency and advection terms are obtained using the centered differencing scheme. Note that the MSE budget is not closed and a small residual term (about 10% of the amplitude of MSE tendency term) exists, due to the errors caused by the temporal interpolation of model output and by the use of the centered differencing scheme, which is not the same as the actual advection scheme of the model.

Figure 6 shows regression maps of each term in the MSE budget equation. Note that surface sensible heat flux and shortwave radiative heating terms are not shown as their magnitude is much smaller than those of the other terms in equation (2). The MSE tendency (contours) features increasing MSE anomalies, which is mostly due to moistening (not shown), to the east of enhanced convection and decreasing to the west. While the magnitude is relatively small, horizontal advection shows a positive (negative) tendency to the west (east) of enhanced convection, suggesting that horizontal moisture advection slows the eastward propagation of the ISO mode. The drying tendency to the east of enhanced convection is possibly caused by the advection of dry air from the region with suppressed convection to the moist region with enhanced convection (Figure 5). The overall weak intensity of horizontal advection likely results from the lack of zonal and meridional gradients in the climatology (Figure 1).

Vertical advection of MSE provides a strong moistening tendency in the columns with enhanced convection and in the region surrounding it. This moistening is associated with the vertical gradient of moisture and strong upward motion in convection. Away from the center of enhanced convection, vertical advection associated with downward motion creates a strong drying tendency. Condensation exhibits the opposite phase to that of vertical advection. It produces a drying tendency in the place with strong updrafts due to condensation, a moistening tendency in the place with subsidence due to suppressed condensation.

Figure 6d shows that the moistening to the east of and drying to the west of the enhanced convection is dominated by surface evaporation. In fact, horizontal distribution of the anomalous surface latent heat flux is almost identical to that of the total tendency. And the magnitude of surface latent heat flux in the areas of large tendencies is much larger than that of the other terms. This result strongly suggests that the eastward propagation of the ISO mode is driven by the surface latent heat flux anomalies.

4. Mechanism Denial Experiments

In this section, we examine results from the mechanism denial experiments (section 2.3) in order to seek a deeper understanding of the dynamics of the simulated ISO mode in our control simulation. Figure 7 shows the climatological mean distribution of precipitable water and precipitation in all simulations. Except for the Fixed_tau simulation, which exhibits slightly more precipitable water than other simulations, all simulations have a similar amount of precipitable water in the tropics with a weak meridional gradient of precipitable water in the deep tropics.

Figure 8 shows the space–time spectra of equatorial precipitation in the mechanism denial experiments. The spectrum of the control simulation is shown again as a reference. The spectrum of Fixed_tau resembles that of the control simulation; intraseasonal variability in the Fixed_tau experiment remains dominated by an eastward propagating, wave number-1 mode with a period of about 60 days. This suggests that the
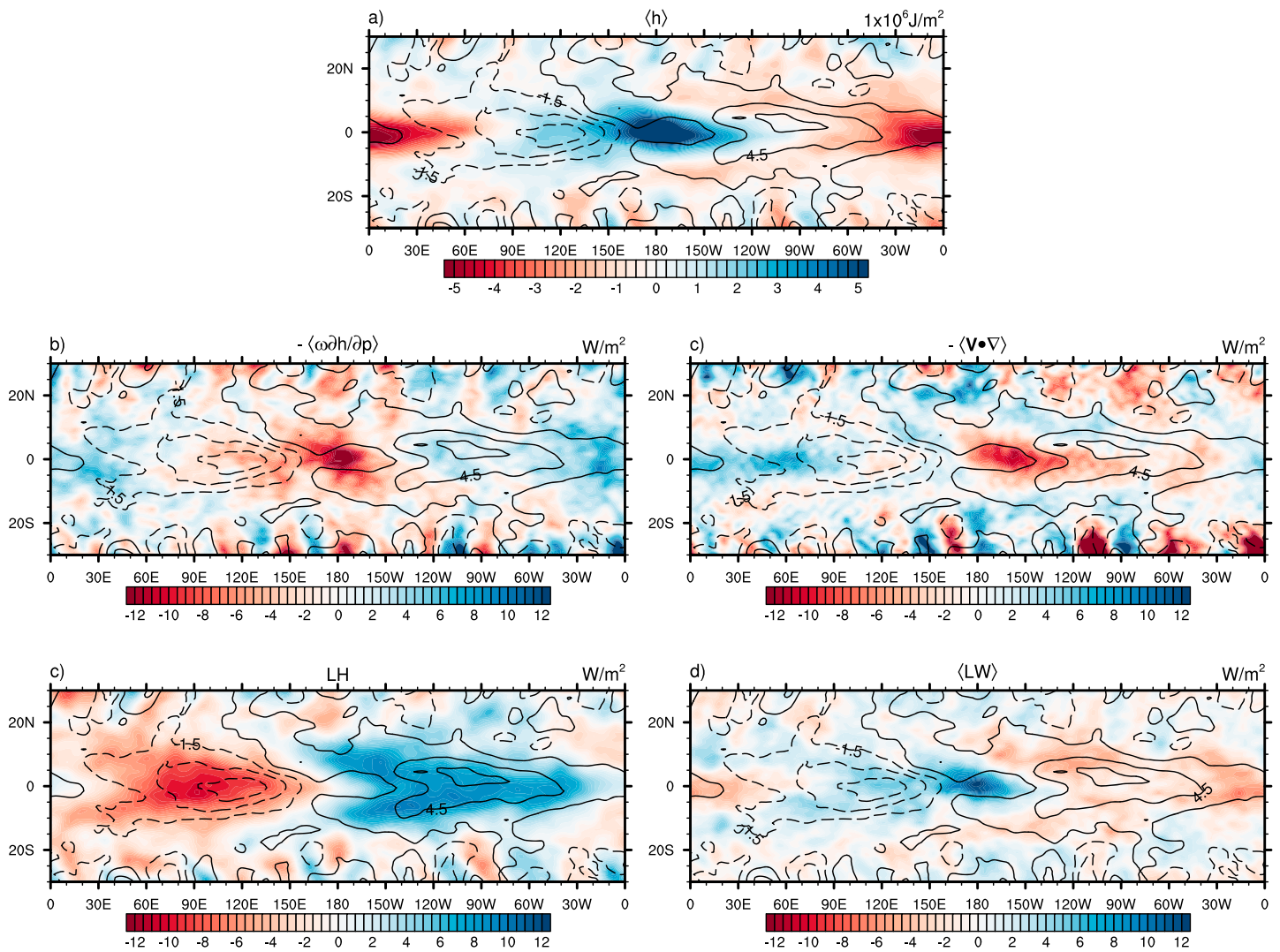
Figure 6. MSE tendency (contours) and various MSE budget terms (shaded) regressed onto the ISV index in the control simulation. (a) MSE anomalies, (b) horizontal advection, (c) vertical advection, (d) surface latent heat flux, and (e) column-integrated longwave radiative heating. MSE = moist static energy; ISV = intraseasonal variability.
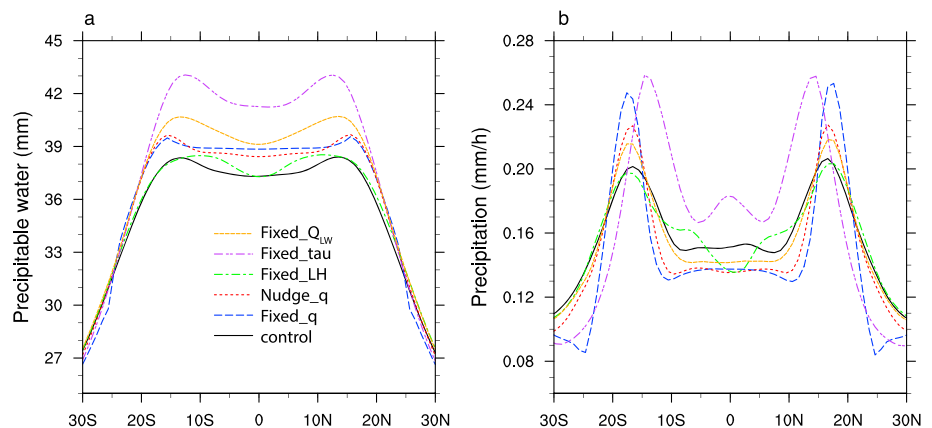

Figure 7. Time mean, zonal mean (a) precipitable water and (b) precipitation rate in all simulations.
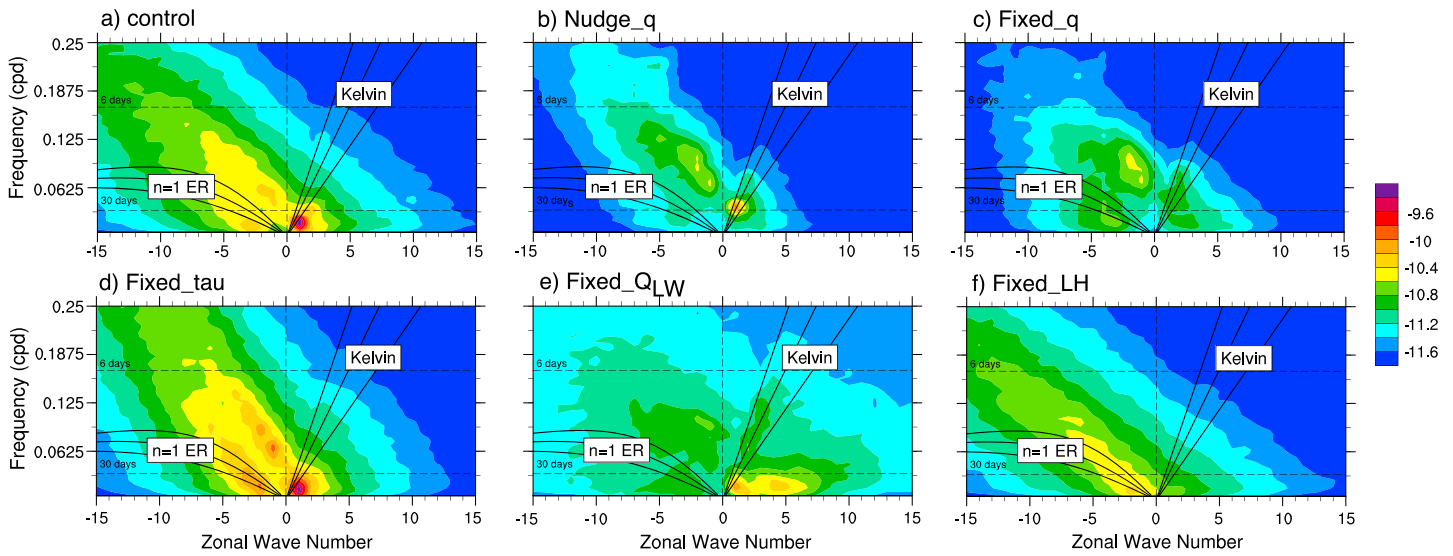
Figure 8. Space-time spectra of the symmetric component of precipitation within 15°S and 15°N in the simulations.

interaction between lower-tropospheric circulation and surface wind stress is not the key mechanism governing the simulated ISO in the control simulation.

The Fixed_Q_{LW} simulation exhibits a significant change in the spectrum. Its intraseasonal variability is still dominated by eastward propagating waves, but the variability is spread over a wide wave number band from wave number 1 to 6, unlike in the control simulation, in which spectral power is concentrated on the wave number 1. Interestingly, the spectrum shows a dip at wave numbers 2 and 3. This suggests that the longwave cloud-radiation feedback plays an important role in the scale selection of intraseasonal variability, consistent with the theoretical arguments by Adames and Kim (2016). The spectral peak over the band of the convectively coupled Kelvin waves becomes more prominent when compared to the control simulation. D. Kim et al. (2011) also found that turning off the longwave cloud-radiation feedback strengthens the convectively coupled Kelvin wave at the expense of MJO variability.

To test if the longwave cloud-radiation feedbacks in the control simulation are indeed scale selective, we estimate the wave number dependence of the radiative feedback parameter r, which is defined by the following relationship,
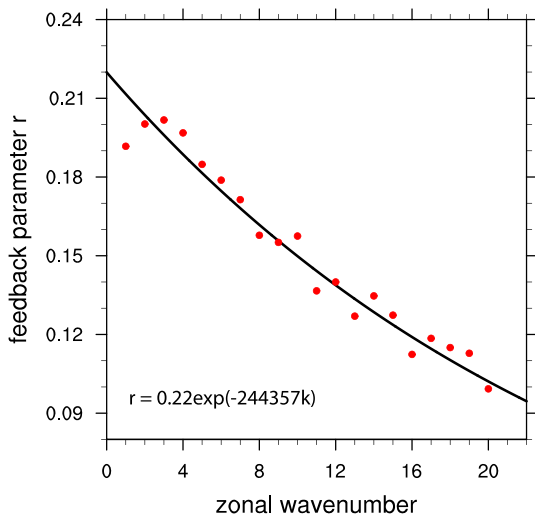
$$R' = rP', \tag{3}$$

where R' and P' are anomalies of outgoing longwave radiation at the top of the atmosphere and precipitation at the surface, respectively. Following Adames and Kim (2016), we decompose the 20- to 100-day filtered R' and P' within 15°S and 15°N into contributions from individual zonal wave numbers and compute r for each wave number through linear least squares regression. Data on each latitude circle are computed, and the averaged feedback parameter as a function of zonal wave number is shown in Figure 9, which suggests that r decreases with wave number in general, and the cloud-radiation feedback is indeed scale selective. The relation between r and zonal wave number k can be depicted by the following empirical formula,

$$r = r_0 e^{-L_r k}. \tag{4}$$

Least squares fitting with data in Figure 9 results in $r_0 = 0.22$ and $L_r = 244$ km, consistent with the estimates of Adames and Kim (2016) using observational data.
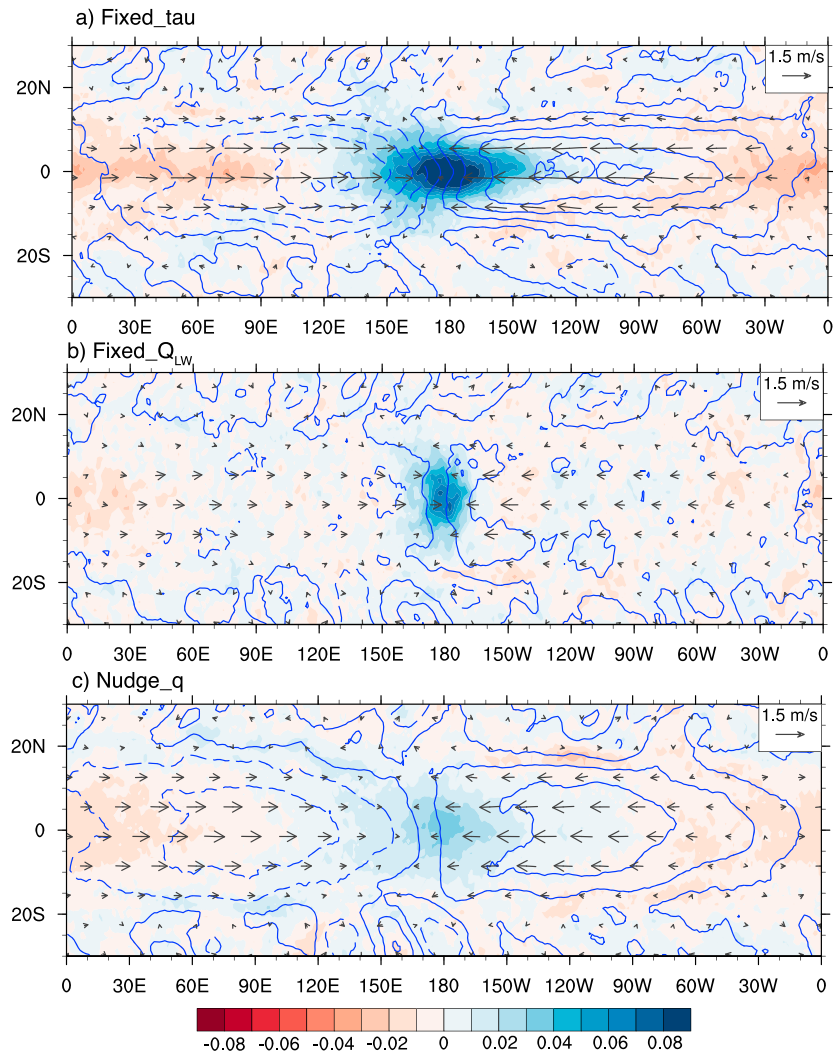

Figure 9. Cloud-radiation feedback parameter r as a function of zonal wave number (red dots). The black solid curve is the linear least squares regression.

Figure 10. The regression map of precipitation (color), 850-hPa wind (vectors), and surface evaporation (contours) onto the intraseasonal variability index time series in the noS, noL, and nuQ simulations. Dashed contours indicate negative values.

However, an intriguing detail of Figure 9 is that the radiative feedback is not strongest at wave number 1; instead, the feedback parameter peaks at wave numbers 2 and 3, while the estimation based on observational data suggests that r is largest at wave number 1 (Adames & Kim, 2016). This disparity may be caused by inaccurate parameterization of convection and clouds in the model or from uncertainty in the calculation of r for each zonal wave number. That the cloud-radiation feedbacks are strongest at wave numbers 2 and 3, not at wave number 1, may also suggest that while cloud-radiation feedback is important for scale selection in the control simulation, some other mechanism, such as the WISHE feedback (Fuchs & Raymond, 2017), coexists to selectively amplify the intraseasonal variance at wave number 1 in the model. Indeed, while the low-frequency variance spreads between wave number 1 to 6 in Figure 8e, wave number 1 still exhibits slightly larger variance than wave numbers 2 and 3, supporting this hypothesis.

In the Nudge_q experiment, in which the free-tropospheric moisture variability is constrained, the wave number-1 mode shows a notable increase in frequency, and a significant drop in variability (Figure 8b). Further increase in frequency and decrease in power are observed when free-tropospheric moisture is not allowed to vary at all in the Fixed_q experiment (Figure 8c). The increase in the phase speed of the dominant ISO mode can also be seen in the space-time power spectrum 850-hPa zonal wind (Figure 10). These findings suggest that the wave-moisture coupling modulates the propagation speed and amplitude of the ISO mode in the control simulation. Note that in the Fixed_LH experiment, the MJO-like ISO mode disappears (Figure 8f).

The intraseasonal variability is dominated by westward propagating components. That disabling WISHE feedback completely shuts off the MJO-like ISO mode with only minimal changes in the background state (Figure 7) strongly suggests that the WISHE feedback is the key mechanism for the maintenance of the MJO-like ISO mode. This may also suggest that the WISHE feedback prefers the wave number-1 mode, which is consistent with the fact that the wave number-1 mode still exists in the Fixed_Q_{LW} simulation. Although, the existence of wave number-1 mode in the Fixed_Q_{LW} simulation may also benefit from the absence of zonal SST gradient, which, according to Maloney et al. (2010), could shift the dominant wave number toward the lower ones.

In Figure 10, the horizontal structures of the ISO modes in the mechanism denial experiments are shown. Note that results from Fixed_LH and Fixed_q are not shown because their regression maps do not show any significant feature due to the lack of dominant wave signal. The Fixed_tau experiment shows a clear wave number-1 structure in circulation, evaporation, and precipitation field. Evaporation leads precipitation by about 90° in longitude. The convergence of low-level wind appears to be purely zonal, and no significant meridional component is shown in the wind field. In contrast, the Fixed_Q_{LW} experiment shows a much smaller scale in the regressed response of precipitation and evaporation. Wind field retains the wave number-1 structure, but the response is much weaker than that in other experiments. Note that Arnold and Randall (2015) also found in their aquaplanet simulations that removing longwave cloud-radiation feedbacks weakens the MJO-like variability. The Nudge_q simulation, on the other hand, exhibits wave number-1 structure in all three fields, albeit the responses are weaker compared with the control simulation (Figure 4b).

Figure 11 shows vertical structures of the dominant ISO modes in the mechanism denial experiments. Again, the Fixed_tau experiment exhibits well-defined wave number-1 structure. Low-level winds converge at the location of enhanced convection, producing strong upward motion and a positive anomaly of specific humidity, and upper winds diverge above the enhanced convection. Strong subsidence exists at the longitudes about 180° away from the enhanced convection, producing a dry anomaly in the corresponding location. Upward motion in the control simulation exhibits a slight eastward tilting with height in the column with enhanced convection, but upward motions in the Fixed_tau run is upright in the center of convection.

The Fixed_Q_{LW} simulation, in contrast, exhibits weaker, more localized response in all fields. The upward motion in Fixed_Q_{LW} tilts westward with height. The moisture anomaly near the center of enhanced convection appears as a narrow plume, and a weak dry anomaly exists to the immediate east of the moist anomaly. The wind field in Fixed_Q_{LW} seems to have wave number-1 structure, but the downward motion to the immediate east of upward motion anomalies is stronger than the downward motion response 180° away. These features all suggest that eliminating radiation feedback leads to a shrinking in the spatial scale of the ISO mode.

As expected, moisture anomalies are much weaker in the Nudge_q experiment than in the control simulation. But the moisture field exhibits well-defined wave number-1 structure, with moist anomaly being in the column with enhanced convection and dry anomaly 180° away. Moisture anomalies tilt westward with height. Temperature anomalies exhibit a pattern similar to that in the control simulation. Wind field in the Nudge_q experiment resembles that of the control simulation, with a clear wave number-1 structure.

5. Discussion

We find that the salient features of the aquaplanet ISO mode in the control simulation resemble that of the WISHE-moisture mode of FR17. FR17 assumed a basic state that has no horizontal moisture gradient. This is similar to our configuration with a flat SST in the deep tropics. This makes horizontal advection of moisture play a negligible role in our aquaplanet ISO mode and in the WISHE-moisture mode of FR17. When a realistic moisture gradient is considered, horizontal advection becomes a dominating mechanism for eastward propagation in a similar moisture mode model of Adames and Kim (2016).

Phase speed of the WISHE-moisture mode of FR17 increases with the moisture relaxation rate (their α parameter), which is equivalent to an inverse of the moisture relaxation time scale. In this sense, waves in our Nudge_q and Fixed_q would experience a shorter relaxation time scale, hence a greater moisture relaxation rate. Indeed, the moisture relaxation time scale, computed with 20- to 100-day band-passed tropical precipitation and precipitable water, in our control, Nudge_q, and Fixed_q simulations are 32.6, 24.6, and 10.4 hr,
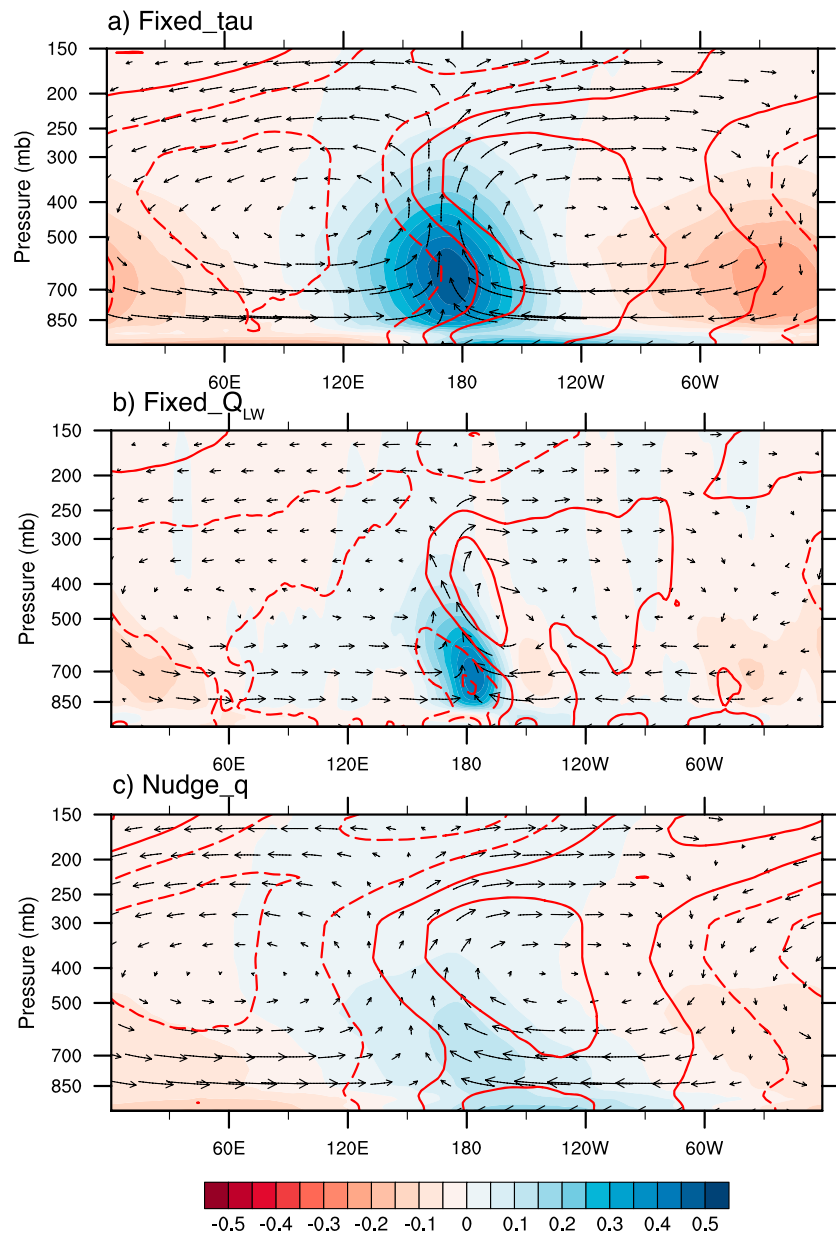
Figure 11. Regression map of mass flux (ρu and ρw), specific humidity (q; color shading), and temperature (T; contours) within 5°S and 5°N onto the time series of ISV index. The unit of q is g/kg. Contour interval for T is 0.1 K; ρw is multiplied by a factor of 250 for better visualization.

respectively. Therefore, the increases in the phase speed of the aquaplanet ISO mode in the Nudged_q and Fixed_q experiments are consistent with what FR17's dispersion relationship of the WISHE-moisture mode predicts.

In the WISHE-moisture mode of FR17, the WISHE mechanism is the only necessary process for instability while the cloud-radiation interaction could also provide an additional amplifying mechanism. In our mechanism denial simulations, the aquaplanet-simulated ISO mode disappears only when the WISHE mechanism is turned off (Fixed_LH). When the longwave cloud-radiation interaction is disabled, the variance of the ISO mode was weakened, and intraseasonal variability still maximizes at wave number 1 (Fixed_Q$_{LW}$), again being consistent with the WISHE-moisture mode of FR17. Unlike the WISHE-moisture mode of FR17, in which the scale selection of a wave number-1 mode is more pronounced without the cloud-radiation interaction
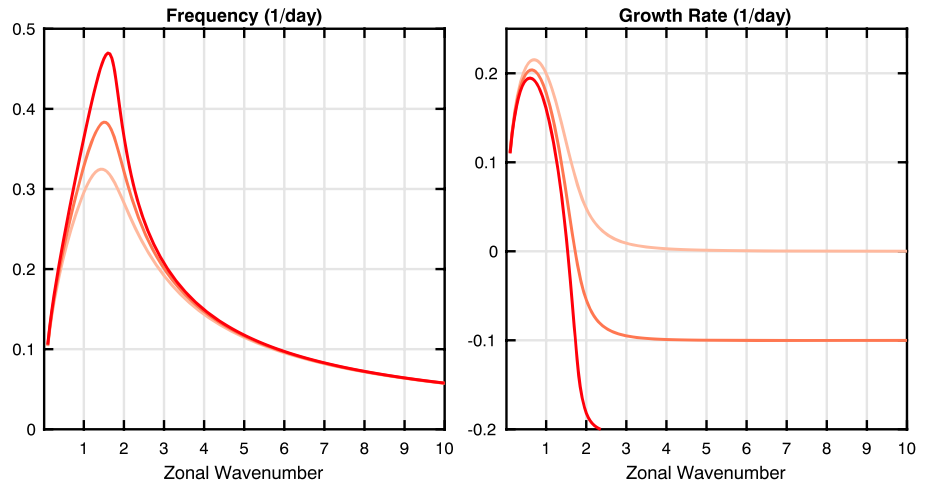
Figure 12. Frequency (left) and growth rate (right) of the growing mode obtained from the dispersion relation in equation (7). The lines correspond to the solutions for Γ^* values of 0, 0.1, and 0.2, respectively. Darker red shading indicates a larger value of Γ^*. All other values used here are as in FR17.

(FR17's Figure 2), however, the results of the Fixed_Q_{LW} experiment suggest that the cloud-radiation feedbacks also play an important role in the scale selection of the aquaplanet ISO mode.

The results from the Nudge_q and Fixed_q experiments can also be shown to be consistent with the FR17 framework. We will modify their moisture equation (equation 11 in FR17) to include the nudging term used in our experiments:

$$\frac{\partial q'}{\partial t} = w' \Gamma_q - s_q - \frac{q'}{\tau_n}.$$

(5)

The right-hand side terms are vertical moisture advection with Γ_q being the vertical moisture gradient, the moisture sources and sinks s_q, and the moisture nudging term where τ_n is a nudging time scale. In this simplified framework, adding the nudging term can be considered as increasing the GMS Γ. We can define a new GMS Γ^* that incorporates the effects of moisture nudging, which is expressed as follows:

$$\Gamma^* = \Gamma + \frac{1}{\tilde{\alpha}\tau_n},$$

(6)

where $\tilde{\alpha}$ is a moisture relaxation time scale, which is inversely proportional to the convective moisture adjustment time scale τ_c (Adames & Kim, 2016, Jiang et al., 2016). The dispersion relation for the $v = 0$ case discussed in FR17 with the new GMS is as follows (their equation 25)

$$\Omega^3 + i\alpha\Omega^2 - \kappa^2\Omega = -\alpha\kappa(\Lambda + i\Gamma^*\kappa),$$

(7)

where Ω is a nondimensional frequency, α is a nondimensional convective relaxation frequency, and κ is a nondimensional zonal wave number. The dispersion relation for values of Γ^* of 0, 0.1, and 0.2 are shown in Figure 12. Consistent with the results from the Nudge_q and Fixed_q experiments (Figure 8), we see that the moist wave accelerates and exhibits weaker growth. Thus, the FR17 model can explain not only the results of the Fixed_LH experiment but also explains results of the Nudge_q and Fixed_q experiments.

6. Summary and Conclusions

In this study, we attempted to understand the nature of intraseasonal variability in an aquaplanet simulation whose spectral character resembles that of the observed MJO. The aquaplanet simulation was performed using GFDL's atmosphere model AM2.1 with a flat SST distribution in the deep tropics. The MJO-like ISO

mode that appeared in the aquaplanet simulation propagates eastward with a period of about 60 days and is spatially dominated by wave number-1 structures. In order to gain insight into the propagation mechanism of the ISO mode, we examined a vertically resolved moisture budget of the ISO mode. We also performed a series of mechanism denial experiments to shed light on the macroscopic feedback processes controlling the wave characteristics of the ISO mode.

The column-integrated MSE budget of the aquaplanet-simulated ISO mode suggested that enhanced surface evaporation to the east of anomalous convection leads the eastward propagation of the ISO mode. Horizontal advection of MSE causes a weak drying tendency to the east of enhanced convection. It is worthwhile to mention that despite their similar wave characteristics, the aquaplanet-simulated ISO mode and the observed MJO show a stark contrast in their moisture budget. Most notably, horizontal advection of MSE causes a weak drying tendency to the east of enhanced convection in the aquaplanet ISO mode, a feature that is distinct from that of the observed MJO, in which horizontal MSE advection plays the dominant role in the propagation of the MJO. Also, enhanced surface evaporation is centered to the east of enhanced convection in the MJO-like ISO mode, while the opposite phase relation is true in the observed MJO. This difference could be a reflection of the mean state differences in the model and observations, or differences in the dynamics. Either difference could potentially explain why AM2.1 does not produce MJO-like variability with a realistic configuration, but produces a strong ISO in the simplified configuration analyzed here.

In the mechanism denial experiments, the interactions of waves with (i) free-tropospheric moisture, (ii) surface wind stress, (iii) longwave radiative heating, and (iv) surface latent heat flux are suppressed or inhibited to illuminate the roles that individual processes play in determining the characteristics of the ISO mode. The results of the mechanism denial experiments are summarized in the following.

- The wave-moisture coupling affects the phase speed of the ISO mode, which increases progressively as the moisture is decoupled from the wave (Nudged_q and Fixed_q).
- The role of surface wind stress is *insignificant*. An MJO-like ISO mode appears even without interactive surface wind stress (Fixed_tau) and its wave characteristics are almost identical to that in the control simulation. This result suggests that frictional moisture convergence is not central to the simulated ISO.
- The longwave radiative feedbacks are essential in the scale selection of the MJO-like ISO mode. When the longwave cloud-radiation feedbacks are disabled (Fixed_Q_{LW}), the intraseasonal variability of precipitation is spread between wave numbers 1 and 6, instead of concentrating on wave number 1. The longwave cloud-radiative feedbacks strength is scale selective in general, as suggested by observations (Adames & Kim, 2016). However, the radiative feedback parameter peaks at zonal wave numbers 2 and 3 in lieu of 1, implying that cloud-radiation feedbacks are not the only mechanism responsible for the scale selection of the ISO mode.
- The surface latent heat flux feedbacks are found to be critical to the aquaplanet-simulated ISO mode, which disappears when surface evaporation is noninteractive (Fixed_LH).

The results of our MSE budget analysis and mechanism denial experiments collectively suggest that the ISO mode in the control simulation is a mode whose existence relies on the surface latent heat flux feedbacks, whose scale is set by the surface latent heat flux and cloud-radiation feedbacks, and whose propagation speed is determined by its coupling with moisture and hence convection. These salient features of the aquaplanet ISO mode resemble that of the WISHE-moisture mode of Fuchs and Raymond (2017). Based on our results, it was hypothesized that the aquaplanet-simulated ISO mode in the control simulation is a manifestation of the WISHE-moisture mode of Fuchs and Raymond (2017).

It is worthwhile to note that the effects of specific feedback processes (e.g., cloud-radiation feedbacks and WISHE) on the simulated ISO mode in a model would be strongly dependent on the way the model represents relevant subgrid-scale processes. For example, the longwave cloud-radiation feedbacks would be stronger if the model convection scheme detrains more water vapor and cloud hydrometeors in the upper levels, if the upper clouds are optically thicker and last longer. Likewise, the strength of WISHE would be affected by the boundary layer and surface flux schemes. Performing the mechanism denial simulations using multiple models would help reduce the uncertainty associated with those in the parameterization schemes.

Aquaplanet simulations have become a popular framework in which one can study atmospheric phenomena in a simpler environment (Blackburn & Hoskins, 2013). The current study presented another example of how

such a framework can be useful in understanding tropical intraseasonal variability. Our results strongly suggest that the WISHE-moisture mode of FR17 exists, while leaving another important question unanswered: Is the aquaplanet-simulated ISO mode a manifestation of the observed MJO or a different mode? If the observed MJO is indeed a WISHE-moisture mode, it probably means that the WISHE feedback is central to the observed MJO, with the cloud-radiation feedback playing a secondary role in the scale selection mechanism. In this case, it is possible that the WISHE feedback is somehow too weak or some other misrepresented circulation details suppress it significantly when AM2.1 is run with realistic configuration, and therefore, the model no longer exhibits the MJO. Another possibility is that the WISHE feedback is not the dominant mechanism for the observed MJO, which implies that the aquaplanet-simulated ISO mode is not exactly a manifestation of the observed MJO. If the eastward propagation of the observed MJO is dominated by some other mechanisms, such as horizontal advection processes which are extremely weak in our aquaplanet simulations, it is impossible to simulate the MJO with our experimental design (flat tropical SST). The lack of the MJO in the simulation with realistic topography and SST can then probably be explained by biases in the horizontal moisture gradient. It is worth noting that a study by Leroux et al. (2016) found that some models are able to simulate ISO when they have a warm pool and not with zonally symmetric SST conditions, suggesting that the horizontal distribution of the boundary condition can influence whether or not a model can represent an MJO-like ISO mode. Further modeling and theoretical studies are warranted to address this important question.

References

Adames, Á. F., & Kim, D. (2016). The MJO as a dispersive, convectively coupled moisture wave: Theory and observations. *Journal of the Atmospheric Sciences*, *73*(3), 913–941. https://doi.org/10.1175/JAS-D-15-0170.1

Adames, Á. F., & Wallace, J. M. (2014). Three-dimensional structure and evolution of the MJO and its relation to the mean flow. *Journal of the Atmospheric Sciences*, *71*(6), 2007–2026. https://doi.org/10.1175/JAS-D-13-0254.1

Adames, Á. F., & Wallace, J. M. (2015). Three-dimensional structure and evolution of the moisture field in the MJO. *Journal of the Atmospheric Sciences*, *72*(10), 3733–3754. https://doi.org/10.1175/JAS-D-15-0003.1

Andersen, J. A., & Kuang, Z. (2012). Moist static energy budget of MJO-like disturbances in the atmosphere of a zonally symmetric aquaplanet. *Journal of Climate*, *25*(8), 2782–2804. https://doi.org/10.1175/JCLI-D-11-00168.1

Anderson, J. L., Balaji, V., Broccoli, A. J., Cooke, W. F., Delworth, T. L., Dixon, K. W., Donner, L. J. (2004). The new GFDL global atmosphere and land model AM2–LM2: Evaluation with prescribed SST simulations. *Journal of Climate*, *17*(24), 4641–4673. https://doi.org/10.1175/JCLI-3223.1

Arnold, N. P., Kuang, Z., & Tziperman, E. (2013). Enhanced MJO-like variability at high SST. *Journal of Climate*, *26*(3), 988–1001. https://doi.org/10.1175/JCLI-D-12-00272.1

Arnold, N. P., & Randall, D. A. (2015). Global-scale convective aggregation: Implications for the madden-Julian oscillation. *Journal of Advances in Modeling Earth Systems*, *7*, 1499–1518. https://doi.org/10.1002/2015MS000498

Blackburn, M., & Hoskins, B. J. (2013). Context and aims of the Aqua-Planet Experiment. *Journal of the Meteorological Society of Japan. Ser. II*, *91*, 1–15.

Bony, S., & Emanuel, K. A. (2005). On the role of moist processes in tropical intraseasonal variability: Cloud–radiation and moisture–convection feedbacks. *Journal of the Atmospheric Sciences*, *62*(8), 2770–2789. https://doi.org/10.1175/JAS3506.1

Bretherton, C. S., Peters, M. E., & Back, L. E. (2004). Relationships between water vapor path and precipitation over the tropical oceans. *Journal of Climate*, *17*(7), 1517–1528. https://doi.org/10.1175/1520-0442(2004)017<1517:RBWVPA>2.0.CO;2

Chao, W. C., & Chen, B. D. (2001). The role of surface friction in tropical intraseasonal oscillation. *Monthly Weather Review*, *129*(4), 896–904. https://doi.org/10.1175/1520-0493(2001)129<0896:TROSFI>2.0.CO;2

Crueger, T., & Stevens, B. (2015). The effect of atmospheric radiative heating by clouds on the madden-Julian oscillation. *Journal of Advances in Modeling Earth Systems*, *7*, 854–864. https://doi.org/10.1002/2015MS000434

Das, S., Sengupta, D., Chakraborty, A., Sukhatme, J., & Murtugudde, R. (2016). Low-frequency intraseasonal variability in a zonally symmetric aquaplanet model. *Meteorology and Atmospheric Physics*, *128*(6), 697–713. https://doi.org/10.1007/s00703-016-0448-y

Emanuel, K. A. (1987). An air-sea interaction-model of intraseasonal oscillations in the tropics. *Journal of the Atmospheric Sciences*, *44*(16), 2324–2340. https://doi.org/10.1175/1520-0469(1987)044<2324:AASIMO>2.0.CO;2

Emanuel, K. A. (1993). The effect of convective response time on WISHE modes. *Journal of the Atmospheric Sciences*, *50*(12), 1763–1776. https://doi.org/10.1175/1520-0469(1993)050<1763:TEOCRT>2.0.CO;2

Emanuel, K. A., David Neelin, J., & Bretherton, C. S. (1994). On large-scale circulations in convecting atmospheres. *Quarterly Journal of the Royal Meteorological Society*, *120*(519), 1111–1143. https://doi.org/10.1002/qj.49712051902

Fuchs, Ž., & Raymond, D. J. (2017). A simple model of intraseasonal oscillations. *Journal of Advances in Modeling Earth Systems*, *9*, 1195–1211. https://doi.org/10.1002/2017MS000963

Grabowski, W. W. (2003). MJO-like coherent structures: Sensitivity simulations using the cloud-resolving convection parameterization (CRCP). *Journal of the Atmospheric Sciences*, *60*(6), 847–864. https://doi.org/10.1175/1520-0469(2003)060<0847:MLCSSS>2.0.CO;2

Hayashi, Y. Y., & Sumi, A. (1986). The 30-40 day oscillations simulated in an" aqua planet" model. *Journal of the Meteorological Society of Japan. Ser. II*, *64*(4), 451–467.

Hsu, P., & Li, T. (2012). Role of the boundary layer moisture asymmetry in causing the eastward propagation of the Madden–Julian oscillation. *Journal of Climate*, *25*(14), 4914–4931. https://doi.org/10.1175/JCLI-D-11-00310.1

Hsu, P., Li, T., & Murakami, H. (2014). Moisture asymmetry and MJO eastward propagation in an aquaplanet general circulation model. *Journal of Climate*, *27*(23), 8747–8760. https://doi.org/10.1175/JCLI-D-14-00148.1

Jiang, X., Zhao, M., Maloney, E. D., & Waliser, D. E. (2016). Convective moisture adjustment time scale as a key factor in regulating model amplitude of the Madden-Julian Oscillation. *Geophysical Research Letters*, *43*, 10,412–10,419. https://doi.org/10.1002/2016GL070898

Kang, I., Liu, F., Ahn, M., Yang, Y., & Wang, B. (2013). The role of SST structure in convectively coupled Kelvin–Rossby waves and its implications for MJO formation. *Journal of Climate*, *26*(16), 5915–5930. https://doi.org/10.1175/JCLI-D-12-00303.1

Kim, D., Kug, J.-S., & Sobel, A. H. (2014). Propagating versus nonpropagating Madden–Julian oscillation events. *Journal of Climate*, *27*(1), 111–125. https://doi.org/10.1175/JCLI-D-13-00084.1

Kim, D., Sobel, A. H., & Kang, I.-S. (2011). A mechanism denial study on the Madden-Julian oscillation. *Journal of Advances in Modeling Earth Systems*, *3*, M12007. https://doi.org/10.1029/2011MS000081

Kim, Y.-J., Giraldo, F. X., Flatau, M., Liou, C.-S., & Peng, M. S. (2008). A sensitivity study of the Kelvin wave and the Madden-Julian Oscillation in aquaplanet simulations by the Naval Research Laboratory Spectral Element Atmospheric Model. *Journal of Geophysical Research*, *113*, D20102. https://doi.org/10.1029/2008JD009887

Lee, M. I., Kang, I. S., Kim, J. K., & Mapes, B. E. (2001). Influence of cloud-radiation interaction on simulating tropical intraseasonal oscillation with an atmospheric general circulation model. *Journal of Geophysical Research*, *106*(D13), 14,219–14,233. https://doi.org/10.1029/2001JD900143

Leroux, S., Bellon, G., Roehrig, R., Caian, M., Klingaman, N. P., Lafore, J. P., et al. (2016). Inter-model comparison of subseasonal tropical variability in aquaplanet experiments: Effect of a warm pool. *Journal of Advances in Modeling Earth Systems*, *8*, 1526–1551. https://doi.org/10.1002/2016MS000683

Lin, S.-J. (2004). A "vertically Lagrangian" finite-volume dynamical core for global models. *Monthly Weather Review*, *132*, 2293–2307. https://doi.org/10.1175/1520-0493(2004)132,2293:AVLFDC.2.0.CO;2

Madden, R. A., & Julian, P. R. (1971). Detection of a 40–50 day oscillation in the zonal wind in the tropical Pacific. *Journal of the Atmospheric Sciences*, *28*(5), 702–708. https://doi.org/10.1175/1520-0469(1971)028<0702:DOADOI>2.0.CO;2

Madden, R. A., & Julian, P. R. (1972). Description of global-scale circulation cells in the tropics with a 40–50 day period. *Journal of the Atmospheric Sciences*, *29*(6), 1109–1123. https://doi.org/10.1175/1520-0469(1972)029<1109:DOGSCC>2.0.CO;2

Majda, A. J., & Stechmann, S. N. (2009). The skeleton of tropical intraseasonal oscillations. *Proceedings of the National Academy of Sciences*, *106*(21), 8417–8422.

Maloney, E. D., & Sobel, A. H. (2004). Surface fluxes and ocean coupling in the tropical intraseasonal oscillation. *Journal of Climate*, *17*(22), 4368–4386. https://doi.org/10.1175/JCLI-3212.1

Maloney, E. D., Sobel, A. H., & Hannah, W. M. (2010). Intraseasonal variability in an Aquaplanet general circulation model. *Journal of Advances in Modeling Earth Systems*, *2*, 5. https://doi.org/10.3894/JAMES.2010.2.5

Moorthi, S., & Suarez, M. J. (1992). Relaxed Arakawa-Schubert: A parameterization of moist convection for general circulation models. *Monthly Weather Review*, *128*(4), 1070–1088. https://doi.org/10.1175/1520-0493(2000)128<1070:ASFCOT>2.0.CO;2

Myers, D. S., & Waliser, D. E. (2003). Three-dimensional water vapor and cloud variations associated with the Madden–Julian oscillation during Northern Hemisphere winter. *Journal of Climate*, *16*(6), 929–950. https://doi.org/10.1175/1520-0442(2003)016<0929:TDWVAC>2.0.CO;2

Neelin, J. D., Held, I. M., & Cook, K. H. (1987). Evaporation-wind feedback and low-frequency variability in the tropical atmosphere. *Journal of the Atmospheric Sciences*, *44*(16), 2341–2348. https://doi.org/10.1175/1520-0469(1987)044<2341:EWFALF>2.0.CO;2

Raymond, D. J., & Fuchs, Ž. (2009). Moisture modes and the Madden–Julian oscillation. *Journal of Climate*, *22*(11), 3031–3046.

Rotstayn, L. D. (1997). A physically based scheme for the treatment of stratiform clouds and precipitation in large-scale models. I: Description and evaluation of the microphysical processes. *Quarterly Journal of the Royal Meteorological Society*, *123*(541), 1227–1282. https://doi.org/10.1002/qj.49712354106

Rotstayn, L. D., Ryan, B. F., & Katzfey, J. J. (2000). A scheme for calculation of the liquid fraction in mixed-phase stratiform clouds in large-scale models. *Monthly Weather Review*, *128*(4), 1070–1088. https://doi.org/10.1175/1520-0493(2000)128<1070:ASFCOT>2.0.CO;2

Shi, X., & Bretherton, C. S. (2014). Large-scale character of an atmosphere in rotating radiative-convective equilibrium. *Journal of Advances in Modeling Earth Systems*, *6*, 616–629. https://doi.org/10.1002/2014MS000342

Shinoda, T., Hendon, H. H., & Glick, J. (1998). Intraseasonal variability of surface fluxes and sea surface temperature in the tropical western Pacific and Indian Oceans. *Journal of Climate*, *11*(7), 1685–1702. https://doi.org/10.1175/1520-0442(1998)011<1685:IVOSFA>2.0.CO;2

Sobel, A. H., & Maloney, E. (2012). An idealized semi-empirical framework for modeling the Madden–Julian oscillation. *Journal of the Atmospheric Sciences*, *69*(5), 1691–1705. https://doi.org/10.1175/JAS-D-11-0118.1

Sobel, A. H., & Maloney, E. (2013). Moisture modes and the eastward propagation of the MJO. *Journal of the Atmospheric Sciences*, *70*(1), 187–192. https://doi.org/10.1175/JAS-D-12-0189.1

Sobel, A. H., Maloney, E. D., Bellon, G., & Frierson, D. M. (2010). Surface fluxes and tropical intraseasonal variability: A reassessment. *Journal of Advances in Modeling Earth Systems*, *2*, 2. https://doi.org/10.3894/JAMES.2010.2.2

Swinbank, R., Palmer, T. N., & Davey, M. K. (1988). Numerical simulations of the Madden and Julian oscillation. *Journal of the Atmospheric Sciences*, *45*(5), 774–788. https://doi.org/10.1175/1520-0469(1988)045<0774:NSOTMA>2.0.CO;2

Tiedtke, M. (1993). Representation of clouds in large-scale models. *Monthly Weather Review*, *121*(11), 3040–3061. https://doi.org/10.1175/1520-0493(1993)121<3040:ROCILS>2.0.CO;2

Wang, B. (1988). Dynamics of tropical low-frequency waves: An analysis of the moist kelvin wave. *Journal of the Atmospheric Sciences*, *45*(14), 2051–2065. https://doi.org/10.1175/1520-0469(1988)045<2051:DOTLFW>2.0.CO;2

Wang, B., & Chen, G. (2017). A general theoretical framework for understanding essential dynamics of madden–Julian oscillation. *Climate Dynamics*, *49*(7–8), 2309–2328. https://doi.org/10.1007/s00382-016-3448-1

Wang, B., & Li, T. (1994). Convective interaction with boundary-layer dynamics in the development of the tropical intraseasonal system. *Journal of the Atmospheric Sciences*, *51*(11), 1386–1400. https://doi.org/10.1175/1520-0469(1994)051<1386:CIWBLD>2.0.CO;2

Wang, B., & Rui, H. (1990). Dynamics of the coupled moist Kelvin-Rossby wave on an equatorial β-plane. *Journal of the Atmospheric Sciences*, *47*(4), 397–413. https://doi.org/10.1175/1520-0469(1990)047<0397:DOTCMK>2.0.CO;2

Yano, J.-I., & Emanuel, K. (1991). An improved model of the equatorial troposphere and its coupling with stratosphere. *Journal of the Atmospheric Sciences*, *48*(3), 377–389. https://doi.org/10.1175/1520-0469(1991)048<0377:AIMOTE>2.0.CO;2

Yasunaga, K., & Mapes, B. (2012). Differences between more divergent and more rotational types of convectively coupled equatorial waves. Part II: Composite analysis based on space–time filtering. *Journal of the Atmospheric Sciences*, *69*(1), 17–34.

Zhang, C. (2013). Madden–Julian oscillation: Bridging weather and climate. *Bulletin of the American Meteorological Society*, *94*(12), 1849–1870. https://doi.org/10.1175/BAMS-D-12-00026.1